



HAL
open science

Giant offshore pumice deposit records a shallow submarine explosive eruption of ancestral Santorini

Timothy H. Druitt, Steffen Kutterolf, Thomas A Ronge, Christian Hübscher, Paraskevi Nomikou, Jonas Preine, Ralf Gertisser, Jens Karstens, Jörg Keller, Olga Koukousioura, et al.

► To cite this version:

Timothy H. Druitt, Steffen Kutterolf, Thomas A Ronge, Christian Hübscher, Paraskevi Nomikou, et al.. Giant offshore pumice deposit records a shallow submarine explosive eruption of ancestral Santorini. *Communications Earth & Environment*, 2024, 5, 10.1038/s43247-023-01171-z . hal-04397778

HAL Id: hal-04397778

<https://uca.hal.science/hal-04397778v1>

Submitted on 16 Jan 2024

HAL is a multi-disciplinary open access archive for the deposit and dissemination of scientific research documents, whether they are published or not. The documents may come from teaching and research institutions in France or abroad, or from public or private research centers.

L'archive ouverte pluridisciplinaire **HAL**, est destinée au dépôt et à la diffusion de documents scientifiques de niveau recherche, publiés ou non, émanant des établissements d'enseignement et de recherche français ou étrangers, des laboratoires publics ou privés.



Distributed under a Creative Commons Attribution 4.0 International License

Giant offshore pumice deposit records a shallow submarine explosive eruption of ancestral Santorini

Tim Druitt¹✉, Steffen Kutterolf², Thomas A. Ronge³, Christian Hübscher⁴, Paraskevi Nomikou⁵, Jonas Preine⁴, Ralf Gertisser⁶, Jens Karstens², Jörg Keller⁷, Olga Koukousioura⁸, Michael Manga⁹, Abigail Metcalfe¹, Molly McCanta¹⁰, Iona McIntosh¹¹, Katharina Pank², Adam Woodhouse¹², Sarah Beethe¹³, Carole Berthod¹⁴, Shun Chiyonobu¹⁵, Hehe Chen¹⁶, Acacia Clark¹⁷, Susan DeBari¹⁸, Raymond Johnston¹⁹, Ally Peccia²⁰, Yuzuru Yamamoto²¹, Alexis Bernard²², Tatiana Fernandez Perez²³, Christopher Jones²⁴, Kumar Batuk Joshi²⁵, Günther Kletetschka²⁶, Xiaohui Li²⁷, Antony Morris²⁸, Paraskevi Polymenakou²⁹, Masako Tominaga³⁰, Dimitrios Papanikolaou⁵, Kuo-Lung Wang³¹ & Hao-Yang Lee³¹

Large explosive volcanic eruptions from island arcs pour pyroclastic currents into marine basins, impacting ecosystems and generating tsunamis that threaten coastal communities and infrastructures. Risk assessments require robust records of such highly hazardous events, which is challenging as most of the products lie buried under the sea. Here we report the discovery by IODP Expedition 398 of a giant rhyolitic pumice deposit emplaced 520 ± 10 ky ago at water depths of 200 to 1000 m during a high-intensity, shallow submarine eruption of ancestral Santorini Volcano. Pyroclastic currents discharged into the sea transformed into turbidity currents and slurries, forming a $>89 \pm 8$ km³ volcanoclastic megaturbidite up to 150 m thick in the surrounding marine basins, while breaching of the sea surface by the eruption column laid down veneers of ignimbrite on three islands. The eruption is one of the largest recorded on the South Aegean Volcanic Arc, and highlights the hazards from submarine explosive eruptions.

¹ University Clermont-Auvergne, CNRS, IRD, OPGC, Laboratoire Magmas et Volcans, Clermont-Ferrand, France. ² GEOMAR Helmholtz Centre for Ocean Research Kiel, Wischhofstrasse 1-3, D-24148 Kiel, Germany. ³ International Ocean Discovery Program, Texas A&M University, College Station, TX 77845, USA. ⁴ Institute of Geophysics, University of Hamburg, Bundesstrasse 55, D-20146 Hamburg, Germany. ⁵ Department of Geology and Geoenvironment, National and Kapodistrian University of Athens, 15784 Athens, Greece. ⁶ School of Geography, Geology and the Environment, Keele University, Keele, Staffordshire ST5 5BG, UK. ⁷ Institut für Geo- und Umweltwissenschaften, Mineralogie - Petrologie, Albertstraße 23b, 79104 Freiburg, Germany. ⁸ School of Geology, Aristotle University of Thessaloniki, 54124 Thessaloniki, Greece. ⁹ Department of Earth and Planetary Science, University of California, Berkeley, CA 94720, USA. ¹⁰ Department of Earth and Planetary Sciences, University of Tennessee, Knoxville, TN 37996-1526, USA. ¹¹ Japan Agency for Marine-Earth Science and Technology, 2-15 Natsushima-cho, Yokosuka, Kanagawa 237-0061, Japan. ¹² Institute for Geophysics, University of Texas, J.J. Pickle Research Campus, Bldg. 196, Austin, TX 78758, USA. ¹³ College of Earth, Ocean, and Atmospheric Sciences, Oregon State University, Corvallis, OR 97333, USA. ¹⁴ Institut De Physique Du Globe De Paris, Centre National de la Recherche Scientifique (CNRS), 75005 Paris, France. ¹⁵ Faculty of International Resource Sciences, Akita University, Akita Prefecture, Akita 0108502, Japan. ¹⁶ School of Ocean Sciences, China University of Geosciences, Haidan District, 100083 Beijing, China. ¹⁷ School of Natural Sciences/CODES, University of Tasmania, Hobart 7005, Australia. ¹⁸ Geology Department, Western Washington University, Bellingham, WA 98225, USA. ¹⁹ School of Geosciences, University of South Florida, Tampa, FL 33620, USA. ²⁰ Lamont-Doherty Earth Observatory, Columbia University, Palisades, NY 10964, USA. ²¹ Graduate School of Science, Kobe University, 1-1 Rokkodai-cho, Nada-ku, Kobe, Hyogo 657-8501, Japan. ²² Laboratoire des Fluides Complexes et leurs Réservoirs, Université de Pau et des Pays de l'Adour, F-64000 Pau, France. ²³ Department of Geology, Kent State University, 221 McGilvrey Hall, 325 S Lincoln Street, Kent, OH 44242, USA. ²⁴ Department of Earth and Planetary Sciences, University of California, Riverside, CA 92506, USA. ²⁵ Solid Earth Research Group, National Centre for Earth Science Studies, Thiruvananthapuram, Kerala 695011, India. ²⁶ Geophysical Institute, University of Alaska Fairbanks, 2156 Koyukuk Drive, Fairbanks, Alaska 99775, USA. ²⁷ Key Laboratory of Submarine Geoscience and Prospecting Techniques, Ocean University of China, Qingdao, China. ²⁸ School of Geography, Earth and Environmental Sciences, Plymouth University, Drake Circus, Plymouth PL4 8AA, UK. ²⁹ Institute of Marine Biology, Biotechnology and Aquaculture, Hellenic Centre for Marine Research, Heraklion, Greece. ³⁰ Department of Geology and Geophysics, Woods Hole Oceanographic Institution, Woods Hole, MA 02543, USA. ³¹ Institute of Earth Sciences, Academia Sinica, Taipei 11529, Taiwan. ✉email: tim.druitt@uca.fr

The processes and impacts of submarine explosive eruptions are poorly understood in comparison to their terrestrial equivalents^{1–5}. However, submarine calderas are common on island arcs^{6,7} and shallow submarine eruptions can be very violent as shown by that of Hunga Tonga–Hunga Ha’apai Volcano in 2022^{8–10}. Pyroclastic currents from such eruptions pour into the sea, entraining water and transforming into water-supported gravity flows^{11–14}. Although the resulting deposits can be studied in ancient successions, those within marine sediments around modern island volcanoes are difficult to access except by deep drilling.

The South Aegean Volcanic Arc lies in the heart of Europe, and its submarine volcanoes are potentially a major hazard^{15,16}. While the eruptive history of the arc has been investigated through onland mapping and marine tephrochronology^{17–19}, the record of submarine volcanism has only been broadly constrained by offshore seismic imagery^{20–23}. In 2022–23, IODP Expedition 398 drilled the marine rifts of the central island arc to depths of up to 900 m below the seafloor in order to ground-truth the seismic stratigraphy, to use the basin sediments as time capsules to recover a complete record of Neogene-Quaternary volcanism, and to seek deposits from past submarine eruptions.

The twelve drill sites lie in and around the Christiana-Santorini-Kolumbo Volcanic Field (CSKVF), which hosts Santorini caldera. The CSKVF is situated within a 100-km-long, NE-SW rift system that cuts across the volcanic arc and consists of three basins (Anhydros, Amorgos, Anafi) containing up to 1400 m of sediments and volcanics above continental basement^{21–24} (Fig. 1). To the south, these basins cut an earlier E-W-trending rift that forms the Christiana Basin^{25–27}. Christiana Volcano has been extinct since ~1.6 Ma²³, and its eroded remnants make up the small islands of Christiani and Askani. Santorini has been active since at least 650 ka, and it last erupted in 1950 CE. Its activity can be grouped geochemically into old (>650–550 ka; ‘Early Centres of Akrotiri’) and young (~530 ka to present day) periods^{17,28}. At least twelve Plinian eruptions have occurred at Santorini since 360 ka, the youngest of which was the ~1600 BCE Minoan eruption: an iconic event in volcanology and archaeology. It was unknown until the present study that major explosive activity took place at the CSKVF before 360 ka¹⁷. Kolumbo Volcano and its chain of submarine cones are located NE of Santorini²⁴. About 70 people were killed on Santorini by the 1650 CE submarine eruption of Kolumbo^{29,30}.

Deep drilling provided us with a unique opportunity to generate a full eruptive time series of the CSKVF, completing a well-studied but incomplete onland story. Additional motivation was provided by a caldera unrest period in 2011–12³¹, and the presence of two shallow magma reservoirs (Santorini and Kolumbo^{32,33}), in a region visited by two million tourists per year. The discovery of the submarine pumice deposit that is the subject of this paper exploited a unique combination of IODP deep drilling, large multidisciplinary shipboard datasets, laboratory analysis, and a dense network of marine seismic profiles.

Results

The submarine eruptive products. The newly discovered deposit, which we call the Archaeos Tuff (Greek: Ancient), was sampled at seven drill sites around Santorini, with core recoveries ranging from <1 to 88 % (Fig. 1; Table 1). It is thickest in cores from the Christiana Basin (65 m, Site U1591; >46 m, Site U1598) and immediately north of Santorini (75 m, Site U1593), of intermediate thickness in the Anafi Basin (50 m, Site U1592; 32 m, Site U1599), and thinnest at the distal end of the Anhydros Basin (8 m, Site U1589). A thin layer occurs atop the horst

separating the Anhydros and Anafi Basins (6 m, Site U1600) (Fig. 2a).

The deposit is composed of massive to diffusely bedded pumice and ash with lesser lithic components (Fig. 3a–e; Supplementary Table 1). Clast-supported pumice lapilli dominate at sites close to Santorini (U1591, U1598, U1593), whereas ash dominates at the most distal site (U1589) (Fig. 3a–e). Grain-size analysis of the deposit is complicated by disturbance effects of drilling and core recovery³⁴ (see Methods); however samples judged to be least affected by core disturbance have median diameters of –1.9 to 3.3 phi, Inman sorting coefficients³⁵ of 1.4 to 2.9 phi, <20 % of sub-63 µm ash, and are better sorted and poorer in fine ash than typical subaerial ignimbrites³⁶ (Fig. 3f, g). With 30–98 wt% of ash (<2 mm) components, the deposits are lapilli tuffs and tuffs (in what follows we use ‘tuff’ for brevity). Most samples are unimodal, but some distal samples (U1589) are bimodal, with coexisting modes of pumice lapilli (2–4 mm) and ash (63–125 µm) (Supplementary Table 2). The deposit is rich in pumice, which comprises almost all of the lapilli (>2 mm) size fraction and dominates the ash fraction. The largest pumice clasts are typically less than a few cm in size and decrease with distance from Santorini (Fig. 2b). Cuts through pumices larger than the drill core diameter (6.2 cm) are very rare. The largest lithic clasts are smaller than pumices at a given site and also decrease in maximum size away from Santorini (Fig. 2b). Lithic lapilli also occur concentrated in rare, cm-thick clast-supported layers within the tuffs (Fig. 3c). An abundance of lithic clasts larger than lapilli size can probably be ruled out because they would have been partially recovered by the drilling.

Pumice clasts are variably angular to rounded. Vesicles comprise 75.9 ± 4.4 vol% of pumice lapilli, with 63.5 ± 7.5 vol % being connected and 12.4 ± 3.8 vol% isolated (Supplementary Table 3), and they range in shape from spherical to tubular. Chemical analyses of the 78 wt% SiO₂ high-silica rhyolite glasses from 38 pumice samples from seven drill sites are mutually identical in terms of major elements, trace elements and incompatible trace element ratios to within analytical uncertainty (Fig. 4; Supplementary Table 4). They are compositionally distinct (e.g., higher Ba/Zr, Ba/Y) from the products of Christiana, Kolumbo, other volcanic fields of the island arc, and young (<530 ka) Santorini¹⁹, and are most similar to those of the Early Akrotiri centres (>650–550 ka) of Santorini (Fig. 4). Phenocrysts comprise a small percentage of the pumices and include plagioclase, quartz, cummingtonite, augite, hypersthene, magnetite, ilmenite and zircon (Supplementary Fig. 1, Tables 5 and 6). Lithic components are mainly lavas, although greenschists (Fig. 3c), limestones and granitoids also occur. Bioclasts picked up from the sea bed are common.

Biostratigraphic constraints on eruption age. Foraminifer and calcareous nannofossil assemblages (Table 2) in sediment layers above the Archaeos Tuff constrain the eruption age at 520 ± 10 ka (Fig. 2a; see Methods). We focus particularly on the upper contact because the lower contact is erosive on some seismic profiles. The biostratigraphic datum for 510 ka (Table 2) lies within \pm a few metres of the upper contact at Sites U1591, U1593, U1599 and U1600, suggesting an eruption age of ~510 ka. The occurrence of this datum immediately below the tuff at Site U1589 could be due to post-eruptive remobilization of the ash-rich material down the basin. Downward extrapolation of sedimentation rates towards the upper contact at Site U1591, using the 467 ka and 510 ka datums in the overlying sediments, gives 520 ± 10 ka for the top of the tuff, the uncertainty arising from the ± 9.5 m depth imprecision on the one-per-core datum levels. The occurrence of the 610 ka datum above the tuff at Site U1592 (Fig. 2a) is

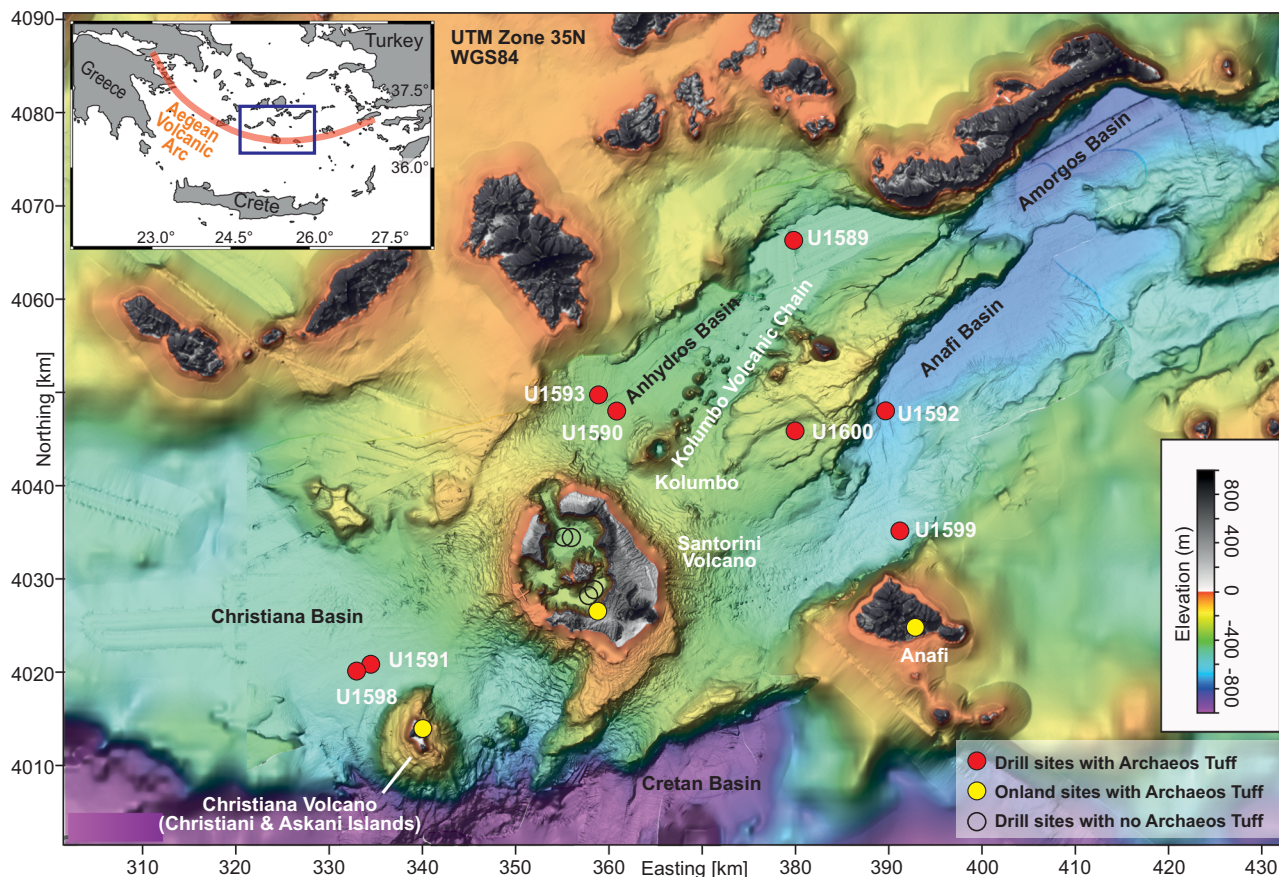


Fig. 1 Occurrences of the Archaeos Tuff. IODP drill sites are shown as red dots and onland sites as yellow dots. The drill sites are labelled with their IODP site numbers. No Archaeos Tuff was in fact recovered at Site U1590, but its presence is seen on seismic profiles. The inset shows the location on the South Aegean Volcanic Arc. See Methods for sources of bathymetric data.

attributed to reworking within an overlying mass flow deposit recognized by its sedimentary characteristics in the cores.

Emplacement water depths. The Archaeos Tuff was emplaced at water depths of several hundreds of metres, comparable to the present-day basin bathymetry. Despite eustatic sea level having been ~50 m lower than the present day at the time of the eruption³⁷, resulting in greater land exposure³⁸, the tuff is intercalated with marine sediments such as oozes and was clearly emplaced under water. Benthic foraminifer assemblages in sediments above and below the deposit constrain the local palaeo-bathymetry prior to, or following, the eruption (see Methods). Palaeowater depths thus inferred are 200–700 m in the Christiana Basin (Site U1591), 500–1000 m along the axis of the Anafafi Basin (U1592), and 200–700 m in the Anhydros Basin (U1589) and at the margin of the Anafafi Basin (U1599) (Supplementary Table 7).

Seismic stratigraphy and volume. The deposit forms an acoustically chaotic to transparent layer on the seismic profiles that can be traced through all the rift basins, ground-truthed by our core-seismic correlation and biostratigraphic ages (Fig. 5; Supplementary Fig. 2). In the Christiana Basin this layer was previously interpreted as a pyroclastic current deposit²⁵ (their seismic Layer III), or as the product of large-scale mass wasting²⁷ (parts U4c and U4d of their seismic Unit U4), but our cores confirm a pyroclastic origin. On a thickness map, the deposit reaches up to 150 m in the basin between Christiana and Santorini as well as in the Anafafi Basin (Fig. 5a). The basal contact is erosive in the

Christiana Basin (Fig. 5b) and on the southeastern flank of Santorini, but conformable at other basin sites.

Integration of the thickness of the tuff across our pre-existing dense array of single channel and multichannel seismic profiles^{21–23,27} yields an observed bulk volume of $89 \pm 8 \text{ km}^3$ using in situ shipboard measurements of P-wave velocity (see Methods). This is the volume contained within the area covered by our seismic network (Fig. 5a) and is a minimum estimate of the total volume. The $\pm 9\%$ uncertainty on the volume arises from that on the P-wave velocity ($1865 \pm 168 \text{ m s}^{-1}$).

Conversion of bulk to DRE (Dense Rock Equivalent) volumes of pyroclastic deposits commonly makes simplified assumptions about the porosity of the uncompacted tuff. In the present study, a unique set of high-resolution shipboard measurements allowed conversion to DRE using real in situ data (see Methods). Shipboard density and pycnometry measurements on 72 core samples of the Archaeos Tuff showed that DRE volume is on average 0.341 ± 0.009 times that of the uncompacted volume (equivalent to a mean deposit porosity of $65.9 \pm 0.9\%$), yielding an observed DRE volume of $30 \pm 3 \text{ km}^3$.

Onland correlatives. Onland outcrops of a geochemically distinctive rhyolitic tuff occurring on Christiani, Santorini, and Anafafi islands (Fig. 1) studied and intercorrelated by Keller et al.^{39,40} can now be attributed to the Archaeos eruption (Supplementary Fig. 3 and Table 8). The outcrops are each a few metres or less in thickness and are of limited extent, so their volume is negligible compared to that of the submarine facies. They consist of poorly sorted (Inman sorting coefficients³⁵ of 3.9

Table 1 Details of sites containing the Archaeos Tuff.

Site	Water depth (mbsl)	Penetration (mbsf)	Holes with Archaeos Tuff	Top of Archaeos Tuff (mbsf)*	Base of Archaeos Tuff (mbsf)*	Thickness of Archaeos Tuff (m)*	% recovery of Archaeos Tuff interval
U1589	484	622	A, B	300	308	8	88
U1591	514	903	A, B	65	130	65	19
U1592	693	528	B	350	400	50	<1
U1593	404	193	A, B	115	190	75	50
U1598	521	99	A, B	61	>107	>46	34
U1599	592	698	A, B	150	182	32	71
U1600	326	189	A, B	37	43	6	58

*Determined by coring and refined from core-seismic correlation in cases of poor core recovery. mbsf: metres below sea floor.

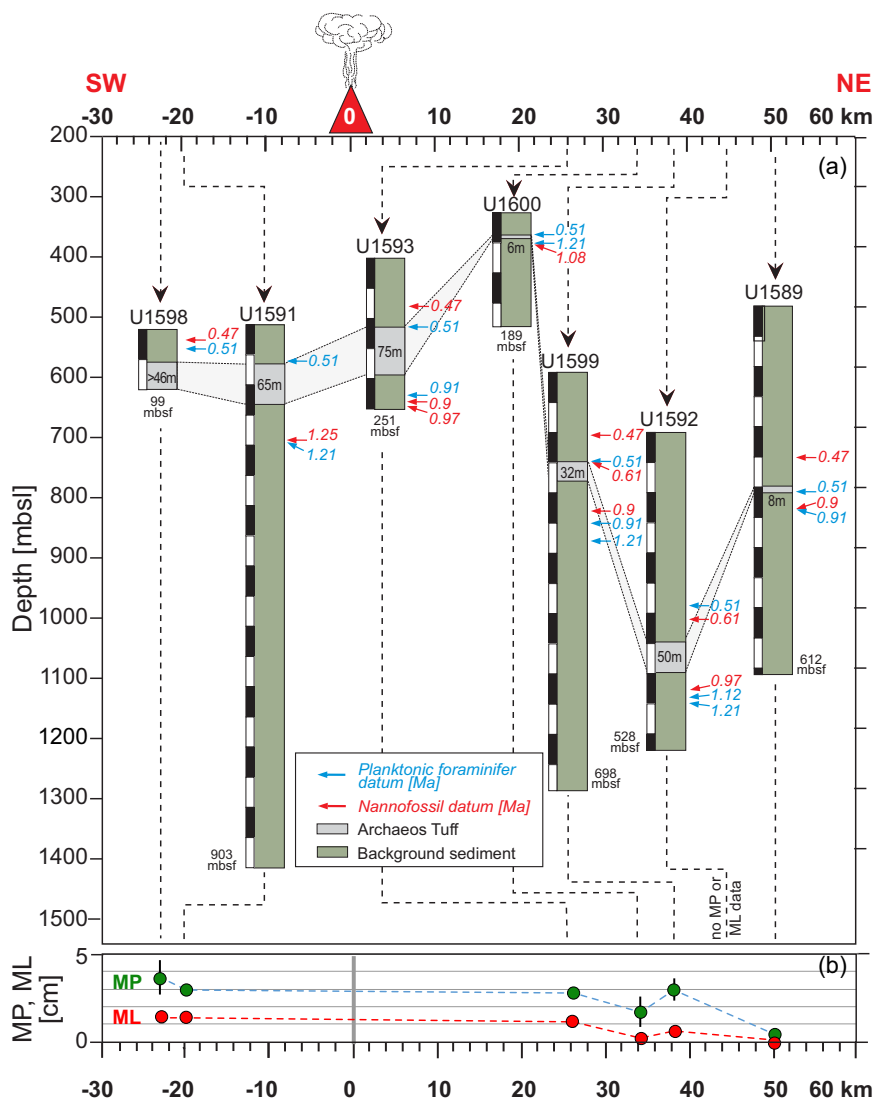


Fig. 2 Biostratigraphic age constraints, thicknesses, depths and maximum clast sizes of the Archaeos Tuff at the different drill sites. **a** Stratigraphic logs. Bathymetric depths are shown with distance from the suspected source. mbsl: metres below sea level. mbsf: metres below sea floor. Ma: million years. Zero distance is arbitrarily taken as the end of the Akrotiri Peninsula on Santorini. **b** Maximum pumice (MP) and maximum lithic (ML) diameters at each site, being the average of the five largest clasts observed on high-resolution core images at each site.

to 4.2) lapilli tuffs with the characteristics of subaerial ignimbrite (Fig. 3f, g; Supplementary Fig. 3, Table 2 and Table 8). On Christiani Island the deposit lies on Pleistocene lavas from Christiana Volcano, and on Santorini and Anafi it lies on metamorphic basement. Maximum lithic clast sizes are ~4 cm on

Anafi, ~9 cm on Santorini and ~1 m on Christiani, the latter occurring as lithic breccia lenses within the ignimbrite. Correlation with the submarine Archaeos Tuff is based on (1) chemically similar glasses and minerals (Supplementary Tables 4–6), (2) the occurrence of cumingtonite, (3) common tubular pumices, and

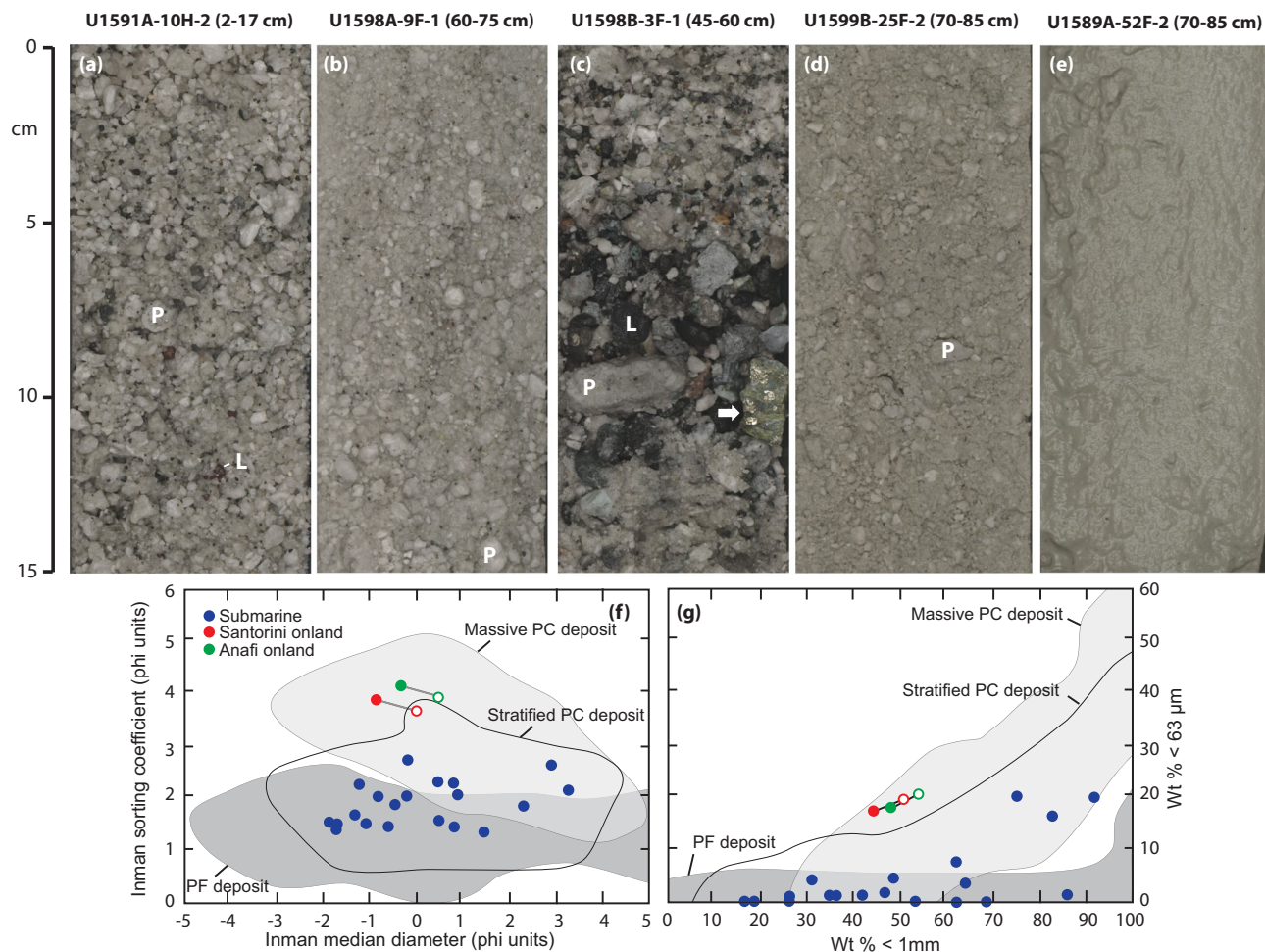


Fig. 3 Textural features of the Archaeos Tuff. **a–e** Representative images of the submarine facies in the IODP cores. Panel **c** shows a lithic-rich segregation layer. P: pumice clast. L: Lithic clast. Arrow marks a greenschist clast rich in epidote and pyrite. U1591A-10H-2 (2–17 cm) means Site U1591, Hole A, Core 10, depth 2–17 cm in core Section 2. H: Advanced Piston Coring (APC); F: Half APC. **f, g** Grain size characteristics of the Archaeos Tuff in core samples judged to be little affected by core disturbance effects³⁴. Two analyses are shown for each onland sample: total sample (dot) and <8 mm size fraction (circle), the latter for comparison with the core samples. The Inman grain size parameters are used³⁵, and the data are compared to fields for the deposits of subaerial pyroclastic currents (PC) and pyroclastic falls (PF)³⁶.

(4) similar lithic assemblages including granitoids and greenschists. The occurrence of cummingtonite is notable; other occurrences of amphibole in the CSKVF belong mostly to the calcic amphibole series (Early Centres of Akrotiri, 1650 CE pumice of Kolumbo, some lavas of Christiana, and very rarely in the Thera pyroclastics^{18,29}), although some Akrotiri tuffs contain cummingtonite coexisting with calcic amphibole (Supplementary Fig. 1).

Discussion

Eruption and emplacement. We interpret the Archaeos Tuff as a volcanoclastic megaturbidite emplaced by a powerful shallow submarine explosive eruption, the column from which collapsed mainly under water (Fig. 6). Fountaining of the eruption column poured pyroclastic currents into the surrounding marine basins, where they transformed into water-supported gravity flows through entrainment of sea water. Breaching of the sea surface by the eruption column also produced subaerial pyroclastic currents that laid down thin layers of ignimbrite on nearby islands. The uniform melt chemistry, distinctive mineral assemblage, and lack of observed depositional breaks favour a single volcanic event. The eruptive intensity must have been very high to explain the

>3000 km² geographic footprint of the submarine deposit and ignimbrite veneers on islands up to 55 km apart. The high vesicularities of pumice lapilli show that magma fragmentation was driven mainly by exsolution of magmatic gases, although components of phreatomagmatic and quench fragmentation in contact with sea water cannot be excluded³⁰.

Submarine deposits from pyroclastic currents can be emplaced by a range of processes, including hot, gas-supported gravity flows, water-supported gravity flows, and fallout from suspension plumes, pumice rafts and pyroclastic currents flowing across the sea^{1,10–14,41–50}. Emplacement of the submarine Archaeos Tuff by gravity flows is implied by its great thickness, thickening into the rift basins, and locally erosional base^{10,12–14}. Fallout from the processes listed above probably accompanied gravity flow emplacement, but cannot have been the dominant emplacement mechanism because it would have produced a thinner, less channelized deposit^{41,44,49,51}. Secondary remobilisation of syn-eruptive deposits, both on the sea floor and from neighbouring islands, may have continued to generate gravity flows after the eruption.

The depositional temperature of the submarine tuff is hard to assess, but the lack of particle sintering textures or any observed

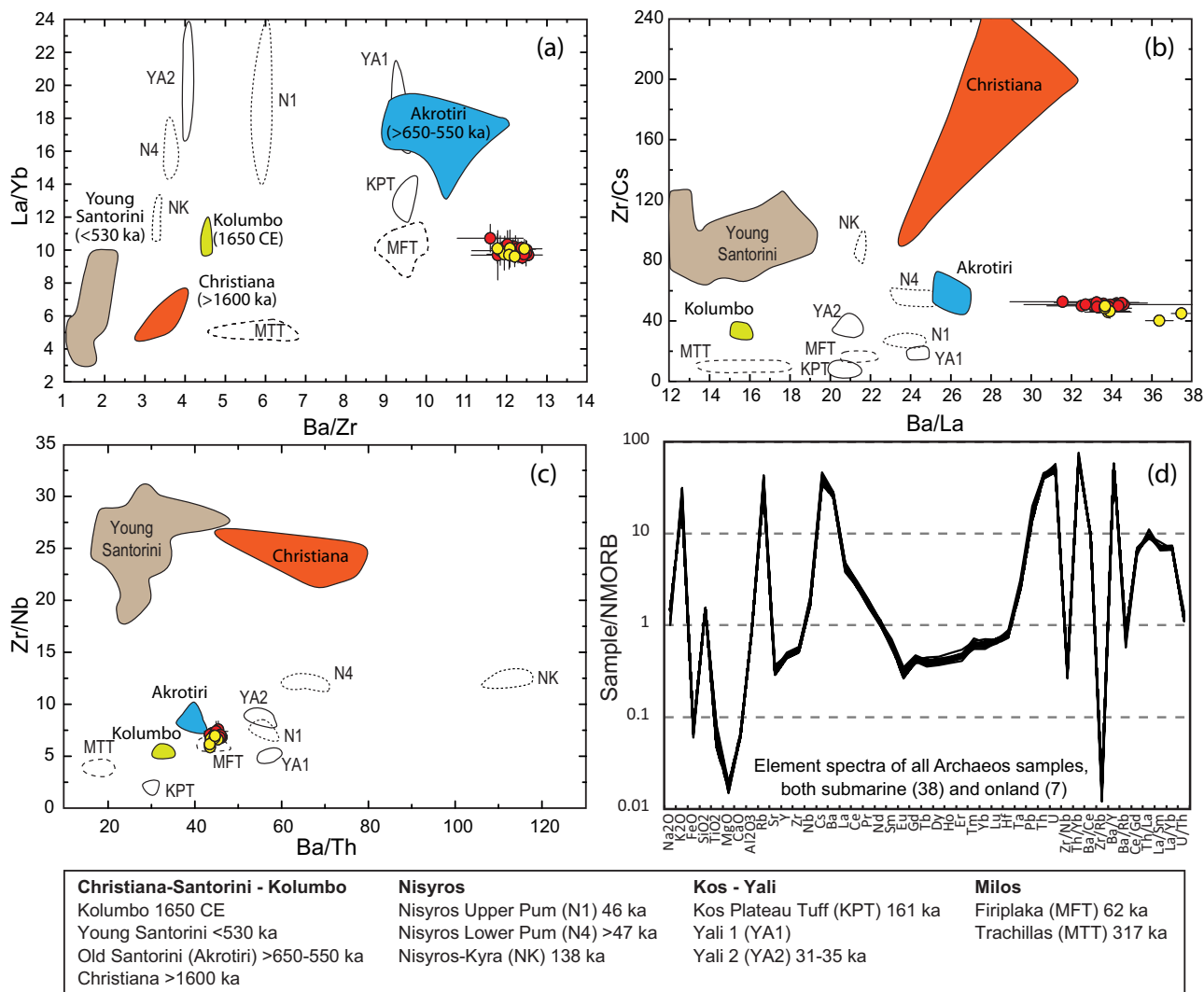


Fig. 4 Chemical compositions of glasses from the Archaeos Tuff. **a-c** Incompatible trace element ratio plots showing the compositional similarity of onland (yellow dots) and offshore (red dots) samples of the Archaeos Tuff to those of the Early Centres of Akrotiri (>650-550 ka), and the differences with other volcanic centres of the South Aegean Volcanic Arc and the younger tuffs of Santorini (<530 ka). Data points denote means and standard deviations. All the analyses are glasses¹⁹, apart from Christiana, which are whole-rock lavas with >60 % SiO₂. **d** Glass element spectra normalized to N-MORB for 38 offshore samples (at seven drill sites shown in red in Fig. 1) and 7 onshore samples (yellow locations in Fig. 1) of the Archaeos Tuff, showing the essentially identical compositions.

Table 2 Biostratigraphic datums used in this paper.

Calcareous Nannofossil events	Reference	Age (ka)
Acme Base <i>Emiliania huxleyi</i> ,	81	50
Base of <i>Emiliania huxleyi</i>	82	265
Top of <i>Pseudoemiliania lacunose</i>	82	467
Top of <i>Gephyrocapsa</i> sp.3	81	610
Top of <i>Reticulofenestra asanoi</i>	82	901
Base of <i>Gephyrocapsa</i> sp.3	81	970
Planktonic foraminifera events		
Base <i>Globigerinoides ruber</i> pink	83	330
Paracme top <i>Neogloboquadrina</i> spp. (sinistral)	83	510
Paracme base <i>Neogloboquadrina</i> spp. (sinistral)	83	910

gas escape pipes probably rules out very hot emplacement from gas-supported flows¹¹ at our drill sites. The moderate to good sorting of the deposit is more consistent with transport in water-supported gravity flows since the higher density and viscosity of water sorts particles of different sizes and densities more

efficiently than gas^{30,41,49}. This probably explains the better sorting and fines depletion of the submarine tuff compared to its onland ignimbrite (Fig. 3f, g). Moreover, the maximum clast sizes of pumices and lithics in the submarine tuff are calculated to be in approximate hydraulic equivalence in water if the connected pore space of the pumices was waterlogged (see Methods), while the moderate to low rounding of the pumice lapilli may be attributed to the lower energy of interparticle impacts in water-supported gravity flows than in gas-supported ones¹²⁻¹⁴. Our observations are consistent with studies of ancient submarine tuffs^{11-14,42-46}, and experiments of flowing hot ash into water⁴⁷, showing that hot pyroclastic currents entering the sea (either from submarine or subaerial vents) rapidly entrain water and transform into turbidity currents, and that submarine deposits from hot gas-particle flows are limited to near-shoreline environments^{11,48}. We envisage a flux of turbidity currents and granular slurries sustained over many hours or days to generate the Archaeos megaturbidite.

Although the evidence favours relatively cold emplacement of the submarine tuff at our drill sites, the abundance of highly

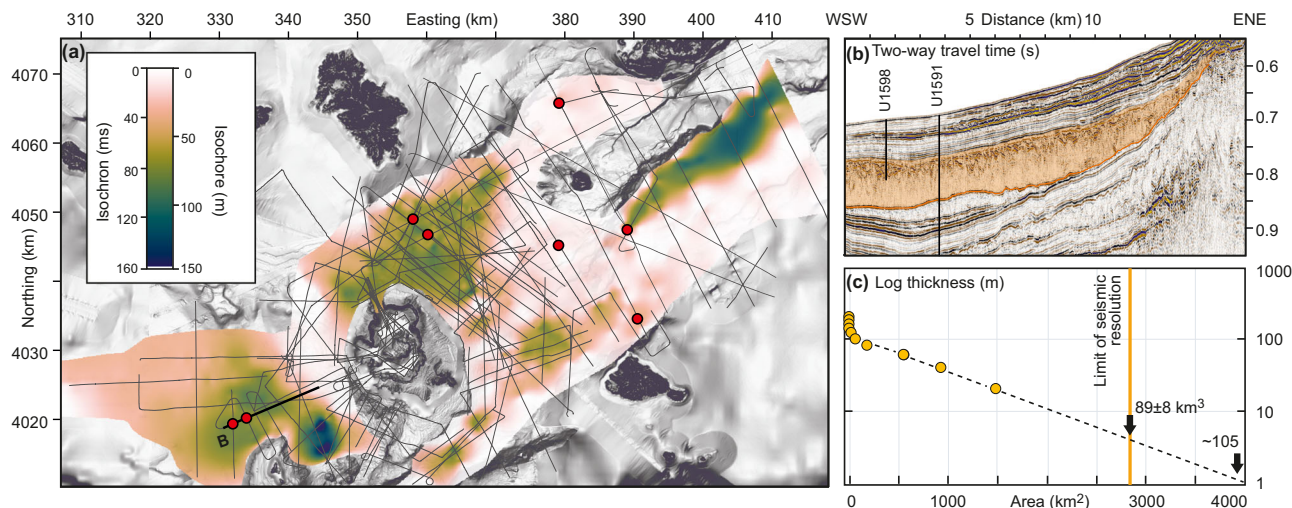


Fig. 5 Distribution and thickness of the Archaeos Tuff from core-seismic integration. **a** Combined two-way travel (TWT) time and thickness map, derived by integration of the drill core stratigraphy with seismic profiles, and conversion to thickness using onboard measurements of P-wave velocity. Red dots are the drill sites. **b** WSW-ENE seismic profile across the Christiana Basin (bold line), showing the Archaeos Tuff in orange. The orange line marks the base of the deposit, which is erosional on the underlying strata in this part of the basin. **c** Plot of $\log(\text{thickness})$ versus cumulative area from (a). Integrating within the boundary on (a) gives a volume of $89 \pm 8 \text{ km}^3$. Extrapolating to 1 m on plot (b) gives $\sim 105 \text{ km}^3$. This extrapolation is based on the known linearity of data on this plot for several subaerial ignimbrites^{63,64}.

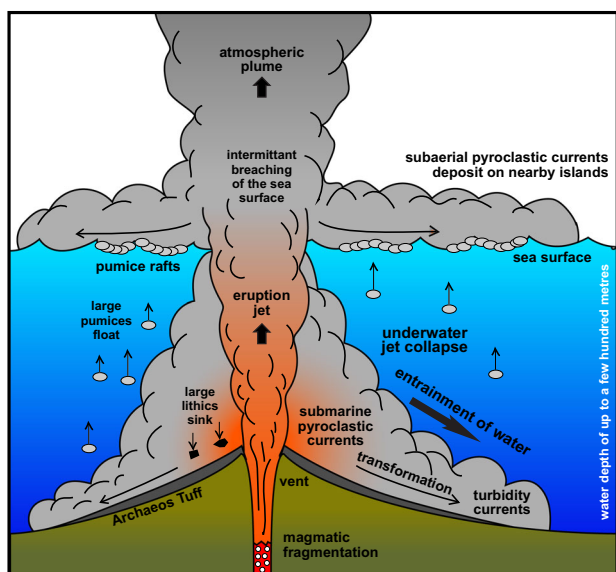


Fig. 6 Schematic depicting eruption and emplacement of the Archaeos Tuff $520 \pm 10 \text{ ky}$ ago. The eruption took place from one or more shallow submarine vents of the ancient Akrotiri Volcano¹⁷ in the Santorini-Christiana area. The vent was situated in water shallow enough for magma fragmentation to occur mainly by the exsolution and expansion of magmatic gases¹. Orange colours in the jet denote higher temperatures. As the gas-particle mixture of the eruption jet rose through the water column, it ingested water and partially collapsed to form submarine pyroclastic currents²⁻⁴. These currents in turn entrained more water and transformed into turbidity currents and slurries that spread out across the sea floor¹¹⁻¹³ laying down a volcanoclastic megaturbidite up to 150 m thick. Breaching of the sea surface by the eruption column also generated subaerial pyroclastic currents that travelled across the sea surface and pumice rafts⁵⁶⁻⁵⁹, and deposited thin veneers of ignimbrite on the islands (not shown) of Christiani, early Santorini, and Anafi. The cartoon is exaggerated vertically, being several km across and about a km high.

vesicular pumice suggests that the initial pyroclastic currents entered the water column at high temperature. While cold pumice floats in water, hot pumices sink and are incorporated into gravity flows because they saturate with water drawn into interconnected vesicles as the magmatic gases thermally contract and change phase^{52,53}. Pumices larger than a few cm are probably scarce because large hot pumices in water take longer to saturate than small ones; they first float to the sea surface forming a pumice raft before later saturating and sinking^{44,52,53}. Any pumice rafts from the eruption must have been dispersed by surface currents⁵⁰, because we have not observed accumulations of large pumices at the top of the tuff at our drill sites⁴⁹. Alternatively, magma fragmentation during the high-intensity eruption may have been sufficiently efficient for pumices larger than lapilli size not to have been produced in any great abundance. Lithic clasts larger than a few cm in size probably fell out of the gravity flows close to source, leaving a sustained flux of turbidity currents and slurries rich in pumice, small lithics and ash to spread out across the sea floor^{13,47}.

Establishing whether a submarine volcanoclastic deposit was erupted from submarine or subaerial vents is difficult⁴⁹, and a combination is of course possible around a large collapsing caldera in a marine environment. Although we cannot completely exclude island vents, the collective evidence favours eruption of the Archaeos Tuff from shallow submarine vents. By ‘shallow’ in this context, we mean less than about $\sim 1 \text{ km}$ water depth where magmatic fragmentation and formation of highly vesicular pumice is possible^{1,4,7}. First, apart from Christiana and the basement precursor island of Santorini¹⁷, little of the CSKVF existed above sea level 520 ky ago. Products older than 520 ka on Santorini are submarine tuffs, subsequently tectonically uplifted. Given that sea level 520 ky ago was only $\sim 50 \text{ m}$ lower than today³⁷, the Archaeos eruptive vents were probably under water. Secondly, thick submarine, eruption-fed megaturbidites rich in well sorted pumice and ash are typical of ‘Neptunian’ explosive eruptions from shallow submarine vents¹³. The pumice-lapilli-rich facies in the Christiana Basin (Sites U1591 and 1598;

Fig. 3a–c) is particularly distinctive in this respect. Thirdly, the great thickness of the Archaeos megaturbidite compared to its onland ignimbrite facies is notable. It contrasts in this respect with Santorini tuffs like the Minoan, which produced thick onland sequences⁵⁴. High-velocity gas-particle jets discharged in shallow submarine eruptions entrain sea water, which can cause the jet to collapse as gravity flows before reaching the surface^{2–4} (Fig. 6). This confines most of the pyroclastic products to the submarine realm, depositing little on nearby islands. For a mass discharge rate typical of large ignimbrite eruptions ($\sim 10^9 \text{ kg s}^{-1}$)⁵⁵, the minimum water depth for jet collapse is $\sim 200 \text{ m}$ ⁴. Taken together, the features of the Archaeos Tuff are most consistent with the eruption of pyroclastic currents from shallow submarine vents.

The presence of poorly sorted ignimbrite on Christiana, Santorini and Anafi islands shows, however, that the upper part of the eruption column breached the sea surface, sending gas-supported pyroclastic currents across the sea. This may have occurred at periods of peak discharge, or later in the eruption once the vent had shallowed^{2,29}. The mechanisms by which pyroclastic currents travel across water and lay down ignimbrite on neighbouring islands have been widely discussed^{56–58}. While we cannot exclude the existence of Middle Pleistocene islands between Christiana and Santorini (where no drill sites are present), our pre-eruption palaeobathymetry data at Site U1599 (200–700 m; Supplementary Table 7) rules out a land bridge extending 30 km eastwards to Anafi. Possibly the subaerial pyroclastic currents were density-stratified and their upper, less dense parts travelled over the sea^{59–62}, or they flowed across pumice rafts during the latter stages of the eruption.

Eruption source. Large-volume pyroclastic currents discharge during caldera-forming eruptions from long-lived polygenetic volcanic complexes. The Archaeos eruption products are compositionally distinct from those of Christiana, Kolumbo, and young (<530 ka) Santorini, and are most similar to those of the old Akrotiri centres (Fig. 4a–c). They also resemble some Akrotiri tuffs in containing cummingtonite. They are not, however, chemically identical to Akrotiri, showing that they represent a similar, but distinct, batch of rhyolitic magma. The Akrotiri products are mainly submarine rhyolitic tuffs that have subsequently been uplifted to $\sim 100 \text{ m}$ above present day sea level¹⁷. We infer that the Archaeos eruption culminated the development of the submarine Akrotiri complex, and this is consistent with our interpretation that the eruption took place from a submarine vent complex. The location of its source caldera is, however, unclear. The caldera may lie buried beneath present-day Santorini, consistent with the broadly symmetrical distribution of the Archaeos Tuff around Santorini. Alternatively, it may have lain in the densely faulted basin between Santorini and Christiana (Fig. 1), which might explain the tuff thickness of up to 150 m in this basin and why the onland ignimbrite is coarsest, with prominent lithic breccia lenses, on Christiana Island. Note that eruption-fed flows sourced between Santorini and Christiana would have had free access into the Anhydros and Anafi Basins because much of subaerial Santorini did not exist at that time¹⁷. Further seismic studies will be required to precisely locate the source caldera.

The $520 \pm 10 \text{ ka}$ age of the Archaeos eruption lies near the transition between the Akrotiri (>650–550 ka) and younger Santorini (<530 ka) periods, which were characterized by geochemically different suites of magmas (Fig. 4a–c). We infer that crustal stress changes immediately preceding or following the Archaeos eruption were sufficiently large to trigger the tapping of new magma batches from storage zones in the crust and mantle.

Implications for the arc. The observed $89 \pm 8 \text{ km}^3$ volume ($30 \pm 3 \text{ km}^3 \text{ DRE}$) of the Archaeos Tuff makes it the largest pyroclastic-current-derived deposit of the CSKVF. It is six times bigger than the pyroclastic current deposit from the Minoan eruption, recently re-evaluated at $14.8 \pm 0.8 \text{ km}^3$ uncompact volume⁵⁴. While the Minoan offshore deposits at Sites U1591 and U1598 are only $\sim 2 \text{ m}$ thick, those of Archaeos are thirty times thicker. Our drilling rules out the formation of any submarine tuffs larger than Archaeos in the history of the CSKVF, since it traversed the entire sedimentary fills of the Anhydros and Anafi Basins to Alpine basement.

Estimating the total volume of products from explosive eruptions is challenging^{63–66}. Owing to our dense seismic network (ground-truthed by drilling) and shipboard core P-wave velocity and density measurements, the volume of the submarine tuff within the zone of study is well constrained. However, $89 \pm 8 \text{ km}^3$ is a minimum estimate of the total eruption volume because it does not take into account (1) distal flow deposits outside of the study area (including any that spilled over into the Cretan basin; Fig. 1), (2) water-suspended and airborne co-ignimbrite ash transported out of the study area, (3) pumice rafts, and (4) intra-caldera tuff. The distal flow volume (1) might be estimated crudely from Fig. 5c, which shows a plot of log (thickness) versus cumulative area. Like subaerial pyroclastic current deposits^{63,64}, the Archaeos data form an approximately linear trend which, when extrapolated to 1 m thickness, yields a volume of $\sim 105 \text{ km}^3$. The other volume components (2 to 4) could significantly increase this, but their contributions cannot be quantified since the record of Middle Pleistocene ash layers in the eastern Mediterranean is sparse^{19,67}, the sizes of any pumice rafts are unconstrained, and the location and size of the source caldera is unknown. It is likely that our minimum volume estimate underestimates the total volume of the Archaeos eruption. Until now the largest eruption of the South Aegean Volcanic Arc has been considered to be the 161 ka Kos Plateau Tuff (KPT)⁶⁸. The DRE volume of the KPT has been estimated as $71 \text{ km}^3 \text{ DRE}$ (including co-ignimbrite ash) using a larger, less well constrained DRE-to-bulk conversion factor¹⁹, but using our factor (which is similar to that determined independently for the Minoan products⁵⁴) decreases it to 42 km^3 . Given the uncertainties, the Archaeos and Kos Plateau eruptions may have been of similar magnitude.

We have documented both the offshore and onshore deposits from a large, shallow submarine explosive eruption, well constrained by volume, age, bathymetric, field and geochemical data, the pyroclastic currents from which were more than ten times larger in volume than the $\sim 6 \text{ km}^3$ of Hunga Tonga–Hunga Ha’apai Volcano in 2022⁹. The findings change our current understanding of the South Aegean Volcanic Arc, revealing a greater capacity for highly hazardous submarine volcanism than previously known. They extend the explosive eruptive history of the CSKVF back in time, reveal a submarine pyroclastic deposit possibly comparable in size to the Kos Plateau Tuff, and imply the existence of a large buried submarine caldera on which the modern volcanic field is founded. The under-representation of the Archaeos Tuff in the subaerial geological record highlights the importance of deep drilling in unravelling the full secrets of island arcs, particularly in densely populated regions like the Mediterranean.

Data and methods

Deep-sea drilling. IODP Expedition 398 took place on the *JOIDES Resolution* from 11 December 2022 to 10 February 2023, and drilled at twelve sites in and around the Christiana-Santorini-Kolumbo Volcanic Field (CSKVF). Details of the seven sites at

which the Archaeos Tuff was recovered are given in Table 1. Two to three holes (A,B,C) were drilled ~50 m apart at each site, and the Archaeos Tuff was intersected in one or more of these holes using either Advanced Piston Coring (9.5 m stroke) or Half-Length Advanced Piston Coring (4.7 m stroke). The core diameters are 6.2 cm. Uncertainties arose in the depth of the top and base of the deposit at some sites due to imperfect core recovery; however subsequent core-seismic correlation allowed these to be precisely determined (Table 1). The standard array of shipboard physical properties measurements were made on the cores (<https://iodp.tamu.edu/labs/index.html>). The cores were logged and described using the standard pyroclastic terminology⁶⁹, taking into account artefacts of drilling and core recovery such as sediment mixing, shear-induced uparching, brecciation, biscuiting and ash liquefaction³⁴. Samples of pumice lapilli and ash were collected from the cores for chemical and mineralogical analysis. Bulk sediment samples were taken from the core catcher of every core for micropalaeontological analysis and determination of biostratigraphic ages and palaeowater depths.

Bathymetry. The digital elevation model (DEM; Fig. 1) was produced by merging satellite-derived Advanced Spaceborne Thermal Emission and Reflection Radiometer (ASTER) data, a community-sourced DEM from the European Marine Observation and Data Network (EMODnet), data acquired on board the *R/V Aegaeo* during the GEOWARN project, and data from the *R/V Marcus G. Langseth* during the PROTEUS seismic tomography project^{15,24,70}. The swath dataset has a lateral resolution of 20 m. It was collected with the SEABEAM 2120 20 kHz swath system onboard *R/V Aegaeo* and with the Simrad Kongsberg EM122 12 kHz multibeam echo sounder on the *R/V Marcus G. Langseth*^{24,70}.

Onland field work. We visited the onland occurrences of the Archaeos Tuff on Christiani, and Santorini and Anafi following earlier studies^{39,71,72}. We restudied the outcrops, and collected new pumice samples for chemical analysis using the same analytical conditions as for the core samples. Keller et al.³⁹ inter-correlated the three occurrences and interpreted the deposit as the product of a major ignimbrite event early in the history of the Santorini volcano group. This interpretation is confirmed by our new findings.

Chemical analysis. Glasses and phenocrysts in pumice lapilli from the onland and submarine facies of the Archaeos Tuff were analysed for correlation purposes. We crushed 2–3 pumice lapilli from each proximal or medial site, but used bulk ash samples from the more distal sites. We sieved the material into grain size fractions with deionized water, embedding the 63–250 μm fraction with epoxy resin into 12 pre-drilled holes in acrylic mounts and polishing to facilitate measurements with the electron microprobe (EMP) and the Laser Ablation Inductively Coupled Plasma Mass Spectrometer (LA-ICP-MS). We also mounted representative phenocryst phases in epoxy.

Major and minor elements of glasses were analysed using a JEOL JXA 8200 wavelength dispersive EMP at GEOMAR, Kiel, using an accelerating voltage of 15 kV, a beam current of 6 nA, and a 10 μm diameter electron beam to minimize sodium loss. Oxide concentrations were determined using the ZAF correction method. Accuracy was monitored by two measurements each on Lipari obsidian⁷³ and Smithsonian basaltic standard VGA99⁷⁴ after every 60 analyses. All analyses with totals of >90 wt% were renormalized to 100% to eliminate the effects of variable post-depositional hydration and minor deviations in focusing of the electron beam. Major and minor element compositions of

amphibole phenocrysts were analyzed by EMP at the University of Tennessee using a 1 μm spot size with a probe current of 30 nA and an accelerating voltage of 15 kV.

Trace element contents of glass shards were analyzed by LA-ICP-MS in two laboratories: the Laboratory of Magmatism and Volcanism in Clermont-Ferrand, France, and at the Academia Sinica in Taipei, Taiwan. Both laboratories used 193 nm Excimer lasers with 24–30 μm beam sizes connected to Agilent 7500 or 7900 ICP-MS instruments. Background was counted for between 20 and 45 s, and samples for between 75 and 100 s. The internal standard was ⁴³Ca, with CaO contents determined by EMP on the same glass shard. The external standard was NIST 612 and the secondary standard was BCR. The GLITTER software was used to reduce the data and calibrate with standards to obtain trace element concentrations. The limit of detection was <100 ppb for most trace elements and ~10 ppb for Rare Earth Elements. The analytical precision was better than 10% for most trace elements. One sample of the Archaeos Tuff was analyzed in both laboratories and the trace element concentrations and ratios were found to be the same within analytical uncertainty.

Textural and grain size measurements. Cores from IODP Expedition 398 rich in pumice and ash such as the Archaeos Tuff were subject to disturbance effects during coring and recovery³⁴. In particular, the ash may in some cases liquefy, allowing some of the finer ash components to decant to the top of each 9.5-m-long core during post-recovery re-sedimentation. Consequently many cores had tops enriched in segregated ash. Fall-in of ash into the drill hole between cores also occurred, resulting in an ash-rich layer at the top of some cores. For these reasons we avoid presenting detailed logs of the cores, which would be misleading. Granulometric analysis is also challenging due to fines segregation within the cores. We addressed this problem by identifying levels in the cores that were little effected by liquefaction: (1) tightly interlocking lapilli and ash which had appeared to have escaped the effect, or (2) intervals of the cores lacking any visible grading in fines content. Twenty such samples (masses 8–82 g) covering the range of lithologies were sieved at 1 phi intervals from –3 to 4 phi.

Connected and isolated vesicularities of pumice lapilli. The connected and isolated vesicularities of twenty representative pumice lapilli in the 1–3 cm size range, collected from the Archaeos Tuff at Sites U1591 and U1598, were measured at the Laboratory of Magmatism and Volcanism in Clermont-Ferrand, France. The lapilli were washed, dried and weighed. The envelope volumes were then measured using a Micromeritics Geopyc 1360 Envelope and T.A.P. Density Analyser. This instrument measures the envelope volume of the lapilli by packing a low-friction granular material around the clast in a reproducible way. The ratio of mass to envelope volume then gave the bulk clast density, which was converted to total vesicularity using a solids density of 2570 kg m^{-3} determined from shipboard measurements (see below). Each clast was then placed in a Micromeritics AccuPyc II 1340 Helium Pycnometer in order to measure the volume of solids plus isolated vesicles. The two datasets were merged to calculate the connected and isolated vesicularities of the lapilli⁷⁵.

Approximate hydraulic equivalence of components. We carried out measurements on high-resolution (<0.1 mm) core images to test whether lithics and waterlogged pumices in the Archaeos Tuff have the same settling velocities in water; i.e., are in hydraulic equivalence. This was done at twelve levels of core sections 398-U1598-9H-1 and 398-U1598-10H-2. In each case, we measured the diameters (mean of length and width) of the five largest

pumice (P) and lithic (L) clasts within a 10 cm height interval, and calculated the average mean maximum diameters D_P and D_L . D_P ranged from 5 to 25 mm with a mean value of 9.6 ± 4.3 mm, and D_L ranged from 1 to 6 mm with a mean value of 2.8 ± 1.2 mm.

Particles of lapilli (>2 mm) size settle through water in the turbulent regime⁷⁶, so a waterlogged pumice and a lithic particle will settle together if $(D_P \Delta \rho_P / D_L \Delta \rho_L)^{0.5} \sim 1$, assuming approximate sphericity⁷⁷. Taking solids density for both (vesicular) pumices and (nonvesicular) lithics as 2570 kg m^{-3} and Mediterranean seawater density as 1030 kg m^{-3} , and denoting total pumice vesicularity as X_{TOT} and isolated pumice vesicularity as X_{ISO} , then we have $\Delta \rho_P \approx 2570(1 - X_{TOT}) + 1030(X_{TOT} - X_{ISO}) - 1030$ and $\Delta \rho_L = 2570 - 1030$. Taking X_{TOT} to be 0.759 and X_{ISO} to be 0.124 (Supplementary Table 3) gives $(D_P \Delta \rho_P / D_L \Delta \rho_L)^{0.5} = 0.77 \pm 0.13$. Given the uncertainties involved in this calculation, the range of pumice vesicularities, and the non-sphericities of the particles (length/width up to 3.3, with a mean value of 1.4), we take this as showing that lithics and waterlogged pumices in the Archaeos Tuff at Site U1598 were in approximate hydraulic equivalence.

Seismic data. The seismic data used in this study are from three cruises between 2006 and 2019^{20,54,78}. Single-channel seismic data were acquired in 2006 during the THERA project on *R/V Aegaeo*. A G-pulser was used as the seismic source, with a volume of 10 in^3 . The general processing comprised simple bandpass filtering (15–500 Hz), de-spiking, predictive deconvolution for the suppression of a strong bubble signal, and spherical divergence correction. In order to migrate the data, we binned the shot points into a regular spacing of 10 m. After migration, we applied a top-mute and white-noise removal. The vertical resolution of these data can be approximated to 8–15 m (using the $\lambda/4$ - or $\lambda/2$ -approximation).

For the cruise POS338 with *R/V Poseidon* in 2006, a GI-pulser was used and operated in true GI mode with a primary (Generator) volume of 45 in^3 and a secondary (Injector) volume of 105 in^3 . Using a 600 m analogue streamer with 24 channels, we defined a common midpoint (CMP) spacing of 12.5 m. Processing of these data comprised trace-editing, simple frequency filtering (10–500 Hz), suppression of a receiver-ghost signal by predictive deconvolution, surface-related multiple elimination as well as spherical divergence correction, pre-stack time migration followed by top-muting and white-noise removal. These data have a main frequency of 60 Hz indicating a vertical resolution of 8–15 m.

During the most recent cruise POS538 in 2019, we acquired seismic data with a much higher lateral resolution (Common Mid-Point spacing of ~ 1.56 m). As a seismic source, we used a GI-pulser that was operated in harmonic mode with primary and secondary volumes of 45 in^3 . Seismic energy was recorded by multiple concatenated Geometrics GeoEel streamer segments, resulting in active streamer sections ranging from 190 m to 250 m in length. Processing comprised trace-editing, simple frequency filtering (15–1500 Hz), and multiple suppression by means of surface-related multiple elimination (SRME). This was followed by spherical divergence correction, time-variant frequency filtering, pre-stack time migration, top-muting, and white-noise removal. With a main frequency of 125 Hz, the vertical resolution is 4–8 m.

All processed seismic profiles were combined into an interpretation project using KingdomSuite software. Here, we established the stratigraphic framework (following published²⁷ nomenclature in all basins, except for the Anhydros Basin, for

which we refined the seismostratigraphy based on new biostratigraphic age markers), mapped seismic units, and created isochron maps (vertical thickness in two-way travel time) by interpolating between the seismic profiles. The Scientific colour map “batlow” is used in this study to prevent visual distortion of the data and exclusion of readers with colour vision deficiencies⁷⁹.

P-wave velocity, core-seismic integration and deposit volume estimation. Integration of core data with seismic profiles requires shipboard measurement of compressional wave (P-wave) velocity. This was measured in situ on wet samples from the working half of split cores using the P-wave gantry system on the *JOIDES Resolution*. Measurements were conducted perpendicular to the core using caliper transducers for every section unless core quality was compromised. For more efficient contact, deionized water was applied on the lower transducer in contact with the core liner. To protect the upper caliper transducer from dirt and damage, a piece of plastic film was placed on the split core surface.

The system uses Panametrics-NDT Microscan delay line transducers, with a frequency of 500 kHz. The distance between the two transducers was measured with a built-in linear variable differential transformer. The P-wave passing through the sample was recorded, and first arrivals were picked as the initial rise of the first peak using an automated procedure. Velocities were manually picked only in circumstances where the automated thresholds did not align with the observed first arrival. The velocity measurement includes a correction for the core liner of known thickness.

A total of 396 discrete P-wave velocity measurements of the Archaeos Tuff were made from five sites and nine holes. The mean velocity is 1864.8 m s^{-1} with a standard error of 0.4 m s^{-1} and a standard deviation of 168.0 m s^{-1} (9 % of the value). We used this velocity to convert the isochron maps to isochore maps (Fig. 5a) in meters and to estimate the bulk volume of the Archaeos Tuff.

Conversion of volume to Dense Rock Equivalent (DRE). The DRE conversion factor is the volume of erupted magma and rock compared to the deposit volume after removing all pore space from vesicles and intergranular voids. The conversion factor can be determined by measuring water content, bulk density, grain density, and solids density from samples recovered by coring using the Moisture and Density facilities on the *JOIDES Resolution*.

A dual balance system was used to measure both wet and dry masses. The two coupled analytical balances, Mettler-Toledo XS204, were used to compensate for the ship motion; one acting as a reference and the other for measurement of the unknown. Before weighing sample-standard pairs, the balances were “tared” to zero based on the mean of 300 measurements; this procedure was performed every 6 hours. Standard weights of similar value to the sample’s weight were placed on the reference balance and the sample was placed on the balance for the unknown mass. Each reported sample mass is the mean of 300 measurements. If the reference and sample masses differed by more than 2 g, the measurement was aborted and then repeated after adjusting the weights on the reference balance. Typically, samples were 10–20 g when wet.

Immediately after samples were collected, the wet sample mass was measured. Dry sample mass and volume were measured after drying the samples in a convection oven for 24 hours at a temperature of $105^\circ \pm 5^\circ \text{C}$ and then cooling them within a desiccator for 3 hours. Dry volume was measured using a shipboard helium-displacement pycnometer with a nominal

precision of $\pm 0.04 \text{ cm}^3$. Each volume value consists of an average of three measurements.

For calculation of sediment bulk density, dry density, grain density, porosity, and void ratio, the traditional ODP method was used⁸⁰ assuming a porewater salinity of 0.035 per mil and density of 1.024 g.cm^{-3} . Because there are isolated vesicles entirely encased by glass in the pumice clasts, the measured grain density can be lower than the density of solids. To account for isolated vesicles, we used the highest measured grain density as an estimate of the solid density (2570 kg m^{-3}).

A total of 74 Moisture and Density samples of the Archaeos Tuff were measured from six sites and nine holes. The mean DRE conversion factor is 0.341 with a standard error of 0.009. Conversion of bulk to DRE volume includes any lithic components in the tuff; however this contribution accounts for no more than a few percent of the volume.

Biostratigraphic ages and palaeobathymetry. Foraminifers and calcareous nannofossils were concentrated from 5–10 cm whole round sediment samples; the majority of samples were taken from core catchers or the bases of cores, but where appropriate additional split-core samples were taken to better define biostratigraphic datums.

Age assignments of studied sections were based on biostratigraphic analyses using calcareous nannofossils and planktonic foraminifers. The 2020 Geologic Time Scale⁸¹ was used and updated with regional biostratigraphic schemes and datums^{82,83}. The biostratigraphic datums within close proximity to the Archaeos Tuff enabled the generation of age-depth models used to approximate the age for the top and base of the tuff, as discussed in the main text.

For calcareous nannofossil analyses, standard smear slide methods were used for all samples using optical adhesive as a mounting medium. The nannofossils were examined under a polarizing light microscope at 1250X magnification. The calcareous nannofossils were classified taxonomically^{82,84}, and genera *Reticulofenestra* was placed into size categories⁸⁵. For the gephyrocapsids, we adopted published concepts⁸² and morphological terminology^{84,86}. Accordingly, *Gephyrocapsa* is divided into four major groups by maximum coccolith length: small *Gephyrocapsa* ($<4 \mu\text{m}$), medium *Gephyrocapsa* (*Gephyrocapsa caribbeanica* and *Gephyrocapsa oceanica*; ≥ 4 but $<5.5 \mu\text{m}$), *Gephyrocapsa* sp. 3 (*Gephyrocapsa parallela*; ≥ 4 but $<5.5 \mu\text{m}$) and large *Gephyrocapsa* (*G. caribbeanica* and *G. oceanica* $\geq 5.5 \mu\text{m}$).

The taxonomy for planktonic foraminifera follows a modified version of the phylogenetic classification⁸⁷, with additional species concepts^{88–90}. Samples were prepared by manually breaking the core into small pieces and soaking in hot water when clay was present. After 5–10 min, samples were disaggregated and washed over a $63 \mu\text{m}$ mesh sieve to remove all mud, silt, and fine sand. The washed microfossil residue retained on the sieve was dried on filter paper in low temperature at $\sim 50^\circ\text{C}$ in a thermostatically controlled drying cabinet and subdivided with a micro-splitter into equal aliquots for examination. As a precaution against cross-contamination, sieves were cleaned with jetted water, placed in an ultrasonic bath for several minutes, dried with compressed air, and thoroughly inspected between samples.

Benthic foraminifer assemblages in the $>125 \mu\text{m}$ grain-size fraction were the primary tool used for estimating palaeowater depths, using published taxonomies^{91–93}. Palaeowater depth ranges were estimated using the deepest calibrated depth marker contained in each sample^{92–97}. The species used (with palaeowater depth ranges in brackets) are *Articulina tubulosa* ($>1000 \text{ m}$), *Cibicides pachyderma* (200–700 m), *Cibicidoides mundulus* ($>1000 \text{ m}$), *Cibicidoides wuellerstorfi* ($>1000 \text{ m}$), *Gyroidina*

soldanii (200–700 m), *Hoeglundina elegans* (50– $>700 \text{ m}$), *Hyalinea balthica* (200–700 m), *Karreriella bradyi* (200–700 m), *Oridorsalis umbonatus* (500– $>1000 \text{ m}$), *Planulina ariminensis* (>50 –700 m), *Trifarina angulosa* (50–700 m), *Trifarina bradyi* (200–700 m), and *Uvigerina peregrina* (>100 –700 m). The complex sedimentary and volcanotectonic settings sampled during IODP Expedition 398 resulted in some uncertainties in palaeowater depth reconstructions through sediment remobilization and downslope displacement of shallow-water species.

Data availability

High-resolution seismic profiles from cruise POS538⁵⁴ can be accessed from Pangea at <https://doi.org/10.1594/PANGAEA.956579>. A selection of vintage seismic profiles^{20,23,27} can be found in the marine geoscience data system (MGDS) at (<https://doi.org/10.26022/IEDA/327525> and <https://doi.org/10.26022/IEDA/331028>). Other data (glass and mineral analyses, grain size analyses, pumice vesicularities, microfossil data, gridded deposit thickness) can be accessed from Zenodo at <https://doi.org/10.5281/zenodo.10060888>.

Received: 13 June 2023; Accepted: 8 December 2023;

Published online: 15 January 2024

References

- White, J. D., Schipper, C. I. & Kano, K. in *The Encyclopedia of Volcanoes* 553–569 (Academic Press, 2015).
- Cahalan, R. C. & Dufek, J. Explosive submarine eruptions: the role of condensable gas jets in underwater eruptions. *J. Geophys. Res. Solid Earth* **126**, e2020JB020969 (2021).
- Hajimirza, S., Jones, T. J., Moreland, W. M., Gonnermann, H. M. & Thordarson, T. Quantifying the water-to-melt mass ratio and its impact on eruption plumes during explosive hydromagmatic eruptions. *Geochem. Geophys. Geosys.* **23**, e2021GC010160 (2022).
- Rowell, C. R., Jellinek, A. M., Hajimirza, S. & Aubry, T. J. External surface water influence on explosive eruption dynamics, with implications for stratospheric sulfur delivery and volcano-climate feedback. *Front. Earth Sci.* **10**, 788294 (2022).
- Gilchrist, J. T., Jellinek, A. M., Hooft, E. E. & Wanket, S. Submarine terraced deposits linked to periodic collapse of caldera-forming eruption columns. *Nat. Geosci.* **16**, 446–453 (2023).
- Fiske, R. S., Naka, J., Iizasa, K., Yuasa, M. & Klaus, A. Submarine silicic caldera at the front of the Izu-Bonin arc, Japan: Voluminous seafloor eruptions of rhyolite pumice. *Geol. Soc. Am. Bull.* **113**, 813–824 (2001).
- Rotella, M. D. et al. Dynamics of deep submarine silicic explosive eruptions in the Kermadec arc, as reflected in pumice vesicularity textures. *J. Volcanol. Geotherm. Res.* **301**, 314–332 (2015).
- Proud, S. R., Prata, A. T. & Schmauf, S. The January 2022 eruption of Hunga Tonga-Hunga Ha’apai Volcano reached the mesosphere. *Science* **378**, 554–557 (2022).
- Seabrook, S. et al. Pyroclastic density currents explain far-reaching and diverse seafloor impacts of the 2022 Hunga Tonga Hunga Ha’apai eruption. *Res. Square* <https://doi.org/10.21203/rs.3.rs-2395332/v1> (2023).
- Clare, M. A. et al. Fast and destructive density currents created by ocean-entering volcanic eruptions. *Science* **381**, 1085–1092 (2023).
- Cas, R. A. & Wright, J. V. Subaqueous pyroclastic flows and ignimbrites: an assessment. *Bull. Volcanol.* **53**, 357–380 (1991).
- Kano, K., Yamamoto, T. & Ono, K. Subaqueous eruption and emplacement of the Shinjima Pumice, Shinjima (Moeshima) Island, Kagoshima Bay, SW Japan. *J. Volcanol. Geotherm. Res.* **71**, 187–206 (1996).
- Allen, S. R. & McPhie, J. Products of Neptunian eruptions. *Geology* **37**, 639–642 (2009).
- Jutzeler, M., McPhie, J. & Allen, S. R. Submarine eruption-fed and resedimented pumice-rich facies: the Dogashima Formation (Izu Peninsula, Japan). *Bull. Volcanol.* **76**, 1–29 (2014).
- Nomikou, P., Papanikolaou, D., Alexandri, M., Sakellariou, D. & Rousakis, G. Submarine volcanoes along the Aegean volcanic arc. *Tectonophysics* **597**, 123–146 (2013).
- Nomikou, P., Hübscher, C. & Carey, S. The Christiana–Santorini–Kolumbo volcanic field. *Elements* **15**, 171–176 (2019).
- Druitt, T. H. et al. Santorini Volcano. *Geol. Soc. London Memoir.* **19**, 165pp (1999).
- Gertisser, R., Preece, K. & Keller, J. The Plinian Lower Pumice 2 eruption, Santorini, Greece: magma evolution and volatile behaviour. *J. Volcanol. Geotherm. Res.* **186**, 387–406 (2009).

19. Kutterolf, S. et al. The medial offshore record of explosive volcanism along the central to eastern Aegean Volcanic Arc: 2. Tephra ages and volumes, eruption magnitudes and marine sedimentation rate variations. *Geochem. Geophys. Geosys.* **22**, e2021GC010011 (2021).
20. Hübscher, C., Ruhnau, M. & Nomikou, P. Volcano-tectonic evolution of the polygenetic Kolumbo submarine volcano/Santorini (Aegean Sea). *J. Volcanol. Geotherm. Res.* **291**, 101–111 (2015).
21. Nomikou, P., Hübscher, C., Ruhnau, M. & Bejelou, K. Tectono-stratigraphic evolution through successive extensional events of the Anydros Basin, hosting Kolumbo volcanic field at the Aegean Sea, Greece. *Tectonophysics* **671**, 202–217 (2016).
22. Nomikou, P. et al. Expanding extension, subsidence and lateral segmentation within the Santorini—Amorgos basins during Quaternary: implications for the 1956 Amorgos events, central-south Aegean Sea, Greece. *Tectonophysics* **722**, 138–153 (2018).
23. Preine, J. et al. Spatio-temporal evolution of the Christiana-Santorini-Kolumbo volcanic field, Aegean Sea. *Geology* **50**, 96–100 (2021).
24. Hooft, E. E. E. et al. Backarc tectonism, volcanism, and mass wasting shape seafloor morphology in the Santorini-Christiana-Amorgos region of the Hellenic volcanic arc. *Tectonophysics* **712–713**, 396–414 (2017).
25. Tsampouraki-Kraounaki, K. & Sakellariou, D. Seismic stratigraphy and geodynamic evolution of Christiana Basin, South Aegean arc. *Marine Geol.* **399**, 135–147 (2018).
26. Heath, B. A. et al. Tectonism and its relation to magmatism around Santorini Volcano from upper crustal P wave velocity. *J. Geophys. Res. Solid Earth* **124**, 10610–10629 (2019).
27. Preine, J. et al. The hidden giant: How a rift pulse triggered a cascade of sector collapses and voluminous secondary mass-transport events in the early evolution of Santorini. *Basin Res.* **34**, 1465–1485 (2022).
28. Francalanci, L. & Zellmer, G. F. Magma genesis at the South Aegean volcanic arc. *Elements* **15**, 65–170 (2019).
29. Cantner, K., Carey, S. & Nomikou, P. Integrated volcanologic and petrologic analysis of the 1650 AD eruption of Kolumbo submarine volcano, Greece. *J. Volcanol. Geotherm. Res.* **269**, 28–43 (2014).
30. Fuller, S., Carey, S. & Nomikou, P. Distribution of fine-grained tephra from the 1650 CE submarine eruption of Kolumbo Volcano, Greece. *J. Volcanol. Geotherm. Res.* **352**, 10–25 (2018).
31. Parks, M. M. et al. From quiescence to unrest: 20 years of satellite geodetic measurements at Santorini volcano, Greece. *J. Geophys. Res. Solid Earth* **120**, 1309–1328 (2015).
32. McVey, B. G. et al. Magma accumulation beneath Santorini volcano, Greece, from P-wave tomography. *Geology* **48**, 231–235 (2020).
33. Chrapkiewicz, K. et al. Magma chamber detected beneath an arc volcano with full-waveform inversion of active-source seismic data. *Geochem. Geophys. Geosys.* **23**, e2022GC010475 (2022).
34. Jutzeler, M. et al. Coring disturbances in IODP piston cores with implications for offshore record of volcanic events and the Missoula megafloods. *Geochem. Geophys. Geosys.* **15**, 3572–3590 (2014).
35. Inman, D. L. Measures for describing the size distribution of sediments. *J. Sediment. Res.* **22**, 125–145 (1952).
36. Walker, G. P. L. Ignimbrite types and ignimbrite problems. *J. Volcanol. Geotherm. Res.* **17**, 65–88 (1983).
37. Spratt, R. M. & Lisiecki, L. E. A late Pleistocene sea level stack. *Clim. Past* **12**, 1079–1092 (2016).
38. Papoulia, C. In *Géarchéologie des Îles de Méditerranée* (eds Ghilardi, M., Leandri, F., Bloemendal, J., Lespez, L., & Fachard, S.) 33–46 (CNRS Editions, 2016).
39. Keller, J., Dietrich, V., Reusser, E., Gertisser, R. & Aarburg, S. Recognition of a major ignimbrite in the early evolution of the Santorini Group: the Christiani Ignimbrite. *Cities on Volcanoes* <https://www.earth-prints.org/bitstream/2122/6924/1/Cities%20on%20Volcanoes%206%20Abstracts%20Volume.pdf> (2010).
40. Keller, J., Gertisser, R., Reusser, E. & Dietrich, V. Pumice deposits of the Santorini Lower Pumice 2 eruption on Anafi island, Greece: Indications for a Plinian event of exceptional magnitude. *J. Volcanol. Geotherm. Res.* **278**, 120–128 (2014).
41. Cashman, K. V. & Fiske, R. S. Fallout of pyroclastic debris from submarine volcanic eruptions. *Science* **253**, 275–280 (1991).
42. Allen, S. R., Freundt, A. & Kurokawa, K. Characteristics of submarine pumice-rich density current deposits sourced from turbulent mixing of subaerial pyroclastic flows at the shoreline: Field and experimental assessment. *Bull. Volcanol.* **74**, 657–675 (2012).
43. Cole, R. B. & Decelles, P. G. Subaerial to submarine transitions in early Miocene pyroclastic flow deposits, southern San Joaquin basin, California. *Geol. Soc. Am. Bull.* **103**, 221–235 (1991).
44. Jutzeler, M. et al. Submarine deposits from pumiceous pyroclastic density currents traveling over water: An outstanding example from offshore Montserrat (IODP 340). *Geol. Soc. Am. Bull.* **129**, 392–414 (2017).
45. Kutterolf, S. et al. Large volume submarine ignimbrites in the Shikoku Basin: An example for explosive volcanism in the Western Pacific during the Late Miocene. *Geochem. Geophys. Geosys.* **15**, 1837–1851 (2014).
46. Trofimovs, J. et al. Submarine pyroclastic deposits formed at the Soufrière Hills volcano, Montserrat (1995–2003): What happens when pyroclastic flows enter the ocean? *Geology* **34**, 549–552 (2006).
47. Freundt, A. Entrance of hot pyroclastic flows into the sea: experimental observations. *Bull. Volcanol.* **65**, 144–164 (2003).
48. Mandeville, C. W., Carey, S., Sigurdsson, H. & King, J. Paleomagnetic evidence for high-temperature emplacement of the 1883 subaqueous pyroclastic flows from Krakatau Volcano, Indonesia. *J. Geophys. Res. Solid Earth* **99**, 9487–9504 (1994).
49. Freundt, A., Schindlbeck-Belo, J. C., Kutterolf, S. & Hopkins, J. L. Tephra layers in the marine environment: a review of properties and emplacement processes. *Geol. Soc. Lond. Spec. Publ.* **520**, 595–637 (2023).
50. Bryan, S. E. et al. Rapid, long-distance dispersal by pumice rafting. *PLoS One* **7**, e40583 (2012).
51. Mitchell, S. J., Fauria, K. E., Houghton, B. F. & Carey, R. J. Sink or float: microtextural controls on the fate of pumice deposition during the 2012 submarine Havre eruption. *Bull. Volcanol.* **83**, 1–20 (2021).
52. Whitham, A. G. & Sparks, R. S. J. Pumice. *Bull. Volcanol.* **48**, 209–223 (1986).
53. Fauria, K. E., Manga, M. & Wei, Z. Trapped bubbles keep pumice afloat and gas diffusion makes pumice sink. *Earth Planet. Sci. Lett.* **460**, 50–59 (2017).
54. Karstens, J. et al. Revised Minoan eruption volume as benchmark for large volcanic eruptions. *Nat. Commun.* **14**, 2497 (2023).
55. Roche, O., Azzaoui, N. & Guillin, A. Discharge rate of explosive volcanic eruption controls runout distance of pyroclastic density currents. *Earth Planet. Sci. Lett.* **568**, 117017 (2021).
56. Carey, S., Sigurdsson, H., Mandeville, C. & Bronto, S. Pyroclastic flows and surges over water: an example from the 1883 Krakatau eruption. *Bull. Volcanol.* **57**, 493–511 (1996).
57. Allen, S. R. & Cas, R. A. Transport of pyroclastic flows across the sea during the explosive, rhyolitic eruption of the Kos Plateau Tuff, Greece. *Bull. Volcanol.* **62**, 441–456 (2001).
58. Dufek, J. & Bergantz, G. W. Dynamics and deposits generated by the Kos Plateau Tuff eruption: controls of basal particle loss on pyroclastic flow transport. *Geochem. Geophys. Geosys.* **8**, 12 (2007).
59. Dufek, J., Wexler, J. & Manga, M. Transport capacity of pyroclastic density currents: experiments and models of substrate-flow interaction. *J. Geophys. Res.* **114**, B11203 (2009).
60. Valentine, G. A. Stratified flow in pyroclastic surges. *Bull. Volcanol.* **49**, 616–630 (1987).
61. Breard, E. C. et al. Coupling of turbulent and non-turbulent flow regimes within pyroclastic density currents. *Nature Geosci.* **9**, 767–771 (2016).
62. Lucchi, F. et al. Sedimentological analysis of ash-rich pyroclastic density currents, with special emphasis on sin-depositional erosion and clast incorporation: the Brown Tuff eruptions (Vulcano, Italy). *Sed. Geol.* **427**, 106040 (2022).
63. Wilson, C. J. N. Ignimbrite morphology and the effects of erosion: a New Zealand case study. *Bull. Volcanol.* **53**, 635–644 (1991).
64. Silleni, A., Giordano, G., Isaia, R. & Ort, M. H. The magnitude of the 39.8 ka Campanian Ignimbrite eruption, Italy: Method, uncertainties and errors. *Front. Earth Sci.* **8**, 543399 (2020).
65. Folkes, C. B. et al. A re-appraisal of the stratigraphy and volcanology of the Cerro Galán volcanic system, NW Argentina. *Bull. Volcanol.* **73**, 1427–1454 (2011).
66. Cook, G. W., Wolff, J. A. & Self, S. Estimating the eruptive volume of a large pyroclastic body: the Otowi Member of the Bandelier Tuff, Valles caldera, New Mexico. *Bull. Volcanol.* **78**, 1–11 (2016).
67. Vakhrameeva, P. et al. The cryptotephra record of the Marine Isotope Stage 12 to 10 interval (460–335 ka) at Tenaghi Philippon, Greece: Exploring chronological markers for the Middle Pleistocene of the Mediterranean region. *Quat. Sci. Rev.* **200**, 313–333 (2018).
68. Allen, S. R., Stadlbauer, E. & Keller, J. Stratigraphy of the Kos Plateau Tuff: product of a major quaternary explosive rhyolitic eruption in the eastern Aegean, Greece. *Int. J. Earth Sci.* **88**, 132–156 (1999).
69. Fisher, R. V. & Schmincke, H.-U. *Pyroclastic Rocks*. (Springer-Verlag, 1984).
70. Nomikou, P., Carey, S. & Papanikolaou, D. Croff Bell, K., Sakellariou, D., Alexandri, M., & Bejelou, K. Submarine volcanoes of the Kolumbo volcanic zone NE of Santorini caldera, Greece. *Glob. Planet. Change* **90–91**, 135–151 (2012).
71. Puchelt, H., Murad, E. & Hubberten, H. W. Geochemical and petrological studies of lavas, pyroclastica and associated xenoliths from the Christiana Islands, Aegean Sea. *Neues Jahrbuch Für Mineralogie-Abhandlungen* **131**, 140–155 (1977).
72. Aarburg, S. & Frechen, M. Die pyroklastischen Abfolgen der Christiana-Inseln (Süd-Ägäis, Griechenland). In Becker-Haumann, R. & Frechen, M. (eds.) *Terrestrische Quartargeologie* 260–276 (Springer, 1999).

73. Hunt, J. B. & Hill, P. G. Tephrological implications of beam size—sample-size effects in electron microprobe analysis of glass shards. *J. Quat. Sci.* **16**, 105–117 (2001).
74. Jarosewich, E., Nelen, J. A. & Norberg, J. A. Reference samples for electron microprobe analysis. *Geostandards Newsletter* **4**, 43–47 (1980).
75. Formenti, Y. & Druitt, T. H. Vesicle connectivity in pyroclasts and implications for the fluidisation of fountain-collapse pyroclastic flows, Montserrat (West Indies). *Earth Planet. Sci. Lett.* **214**, 561–574 (2003).
76. McCave, I. N. Deposition from suspension. In: Sellar, R. C., Cocks, R. & Plimer, R. (eds.) *Encyclopedia of Geology* 5th edn, Vol. 8 (Elsevier, 2005).
77. Burgisser, A. & Gardner, J. E. Using hydraulic equivalences to discriminate transport processes of volcanic flows. *Geology* **34**, 57–160 (2006).
78. Sigurdsson, H. et al. Marine investigations of Greece's Santorini volcanic field. *Eos. Trans. Am. Geophys. Union* **87**, 337–342 (2006).
79. Cramer, F. Scientific colour maps. *Zenodo* <https://doi.org/10.5281/zenodo.1243862> (2018).
80. Blum, P. *Physical Properties Handbook. ODP Tech. Note 26* (ODP, 1997).
81. Raffi, I., Wade, B. S. & Pálke, H. In *Geological Time Scale 2020* (eds Gradstein, F. M., Ogg, J. G., Schmitz, M. D. & Ogg, G. M.) 1141–1200 (Elsevier, 2020).
82. Raffi, I. et al. A review of calcareous nannofossil astrochronology encompassing the past 25 million years. *Quat. Sci. Rev.* **25**, 3113–3137 (2006).
83. Lirer, F. et al. Mediterranean Neogene planktonic foraminifer biozonation and biochronology. *Earth Sci. Rev.* **196**, 102869 (2019).
84. Perch-Nielsen, K. In *Plankton Stratigraphy* 5th edn, Vol. 3 (eds Bolli, H. M., Saunders, J. B. & Perch-Nielsen, K.) 427–554 (Cambridge University Press, 1985).
85. Young, J. R. In *Calcareous Nannofossil Biostratigraphy* 2nd edn, Vol. 3 (ed. Brown, P. R.) 225–265 (Kluwer Academic Publishing, 1999).
86. Takayama, T. & Sato, T. In *Deep Sea Drilling Project Leg 94*. Ruddiman, W. F., Kidd, R. B., Thomas, E. et al. (eds.) Ch. 651–702. (U.S. Govt. Printing Office, 1987).
87. Kennett, J. P. & Srinivasan, M. S. Neogene planktonic foraminifera. *Phylogenet. Atlas* **265**, 546–548 (1983).
88. Huber, B. T. et al. Pforams@ microtax. *Micropaleontology* **62**, 429–438 (2016).
89. Schiebel, R. & Hemleben, C. *Planktonic Foraminifers in the Modern Ocean* (Springer-Verlag, 2017).
90. Lam, A. R. & Leckie, R. M. Late Neogene and Quaternary diversity and taxonomy of subtropical to temperate planktic foraminifera across the Kuroshio Current Extension, northwest Pacific Ocean. *Micropaleontology* **66**, 177–268 (2020).
91. Cimerman, F. & Langer, M. Mediterranean foraminifera. *Academia Scientiarum et Artium Slovenica Classis. Mediterr. Atlas* **30**, 85112 (1991).
92. Sgarella, F. & Moncharmont Zei, M. Benthic foraminifera in the Gulf of Naples (Italy): systematics and autoecology. *Bollet. Della Soc. Paleontol. Italiana* **32**, 145–264 (1993).
93. Rasmussen, T. L. & Thomsen, E. Foraminifera and paleoenvironment of the Plio-Pleistocene Kallithea Bay section, Rhodes, Greece: evidence for cyclic sedimentation and shallow-water sapropels. *Cushman Foundat. Foraminiferal Res. Spec. Publ.* **39**, 15–51 (2005).
94. Wright, R. Neogene paleobathymetry of the Mediterranean based on benthic foraminifers from DSDP leg 42A. *Init. Rep. Deep Sea Drill. Proj. Inst. Oceanogr.* **88**, 837–846 (1975).
95. De Stigter, H. C. & Jorissen, F. J. & Van der Zwaan, G.J. Bathymetric distribution and microhabitat partitioning of live (Rose Bengal stained) benthic foraminifera along a shelf to bathyal transect in the southern Adriatic Sea. *J. Foram. Res.* **28**, 40–65 (1998).
96. De Rijk, S., Troelstra, S. R. & Rohling, E. J. Benthic foraminiferal distribution in the Mediterranean Sea. *J. Foram. Res.* **29**, 93–103 (1999).
97. Milker, Y. et al. Testing the applicability of a benthic foraminiferal-based transfer function for the reconstruction of paleowater depth changes in Rhodes (Greece) during the early Pleistocene. *PLoS One* **12**, e0188447 (2017).

Acknowledgements

This research used samples and data provided by the International Ocean Discovery Program (IODP). We thank the technical staff of the *JOIDES Resolution* for their efforts

in attaining the scientific goals of Expedition 398, and all of the shipboard personnel for a great experience. Special gratitude goes to Bill Rhinehart, Chieh Peng and colleagues in helping us overcome many obstacles and to Katerina Petronotis and the leadership of IODP for their support. We thank the member organizations of IODP for financial aid, IODP France for paying the publication fee, and the Municipality of Thera for help in preparing for the expedition. Shan de Silva, Roberto Sulpizio and an anonymous reviewer provided helpful suggestions for improving the manuscript. This is Laboratory of Excellence ClerVolc contribution 622.

Author contributions

T.D.—Expedition co-chief, data collection, senior author of manuscript. S.K.—Expedition co-chief, data collection, manuscript coauthor. T.A.R.—Expedition Project Manager, manuscript coauthor. C.H.—Project data lead and shipboard scientist. P.N.—Project proponent and shipboard scientist. J.P.—Project co-proponent and shipboard scientist; contributed data and text. R.G.—Shipboard scientist, contributed pre- and post-expedition data and text. J.Ka.—Contributed pre-expedition data. J.Ke.—Contributed pre-expedition data. O.K.—Shipboard scientist, contributed post-expedition data and text. M.Ma.—Shipboard scientist, contributed post-expedition data and text. A.M.—Onshore scientist, contributed post-expedition data. M.Mc.—Shipboard scientist, contributed post-expedition data and text. I.M.—Shipboard scientist, contributed post-expedition data and text. K.P.—Shipboard scientist, contributed post-expedition data and text. Adam Woodhouse—Shipboard scientist, contributed post-expedition data and text. Sarah Beethe—Shipboard scientist. C.B.—Shipboard scientist. S.C.—Shipboard scientist. H.C.—Shipboard scientist. A.C.—Shipboard scientist. S.D.—Shipboard scientist. R.J.—Shipboard scientist. A.P.—Shipboard scientist. Y.Y.—Shipboard scientist. A.B.—Shipboard scientist. T.F.P.—Shipboard scientist. C.J.—Shipboard scientist. K.B.J.—Shipboard scientist. G.K.—Shipboard scientist. X.L.—Shipboard scientist. A.M.—Shipboard scientist. P.P.—Shipboard scientist. M.T.—Shipboard scientist. D.P.—Project proponent. K.-L.W.—Laboratory collaborator. H.-Y.L.—Laboratory collaborator.

Competing interests

The authors declare no competing interests.

Additional information

Supplementary information The online version contains supplementary material available at <https://doi.org/10.1038/s43247-023-01171-z>.

Correspondence and requests for materials should be addressed to Tim Druitt.

Peer review information *Communications Earth & Environment* thanks Roberto Sulpizio, Shanaka de Silva, and the other, anonymous, reviewer(s) for their contribution to the peer review of this work. Primary Handling Editors: Lucia Pappalardo and Joe Aslin. A peer review file is available.

Reprints and permission information is available at <http://www.nature.com/reprints>

Publisher's note Springer Nature remains neutral with regard to jurisdictional claims in published maps and institutional affiliations.



Open Access This article is licensed under a Creative Commons Attribution 4.0 International License, which permits use, sharing, adaptation, distribution and reproduction in any medium or format, as long as you give appropriate credit to the original author(s) and the source, provide a link to the Creative Commons licence, and indicate if changes were made. The images or other third party material in this article are included in the article's Creative Commons licence, unless indicated otherwise in a credit line to the material. If material is not included in the article's Creative Commons licence and your intended use is not permitted by statutory regulation or exceeds the permitted use, you will need to obtain permission directly from the copyright holder. To view a copy of this licence, visit <http://creativecommons.org/licenses/by/4.0/>.

© The Author(s) 2024